

1 Comparison of atmospheric CO₂ mole fractions and 2 source–sink characteristics at four WMO/GAW 3 stations in China

4 Siyang Cheng^{a,*}, Lingxi Zhou^{a,**}, Pieter P. Tans^b, Xingqin An^a,
5 Yunsong Liu^a

6 ^a *State Key Laboratory of Severe Weather, Chinese Academy of Meteorological Sciences*
7 *(CAMS) & Key Laboratory of Atmospheric Chemistry of China Meteorological*
8 *Administration (CMA), Beijing 100081, China*

9 ^b *Earth Systems Research Laboratory, National Oceanic and Atmospheric Administration,*
10 *Boulder, CO, USA*

11 Correspondence to: Siyang Cheng (sycheng@cma.gov.cn), Lingxi Zhou (zhoulx@cma.gov.cn)

12

13 **Abstract**

14 As CO₂ is a primary driving factor of climate change, the mole fraction and source–sink
15 characteristics of atmospheric CO₂ over China are constantly inferred from multi-source and multi-
16 site data. In this paper, we compared ground-based CO₂ measurements with satellite retrievals and
17 investigated the source–sink regional representativeness at China’s four WMO/GAW stations. The
18 results indicate that, firstly, atmospheric CO₂ mole fractions from ground-based sampling
19 measurement and Greenhouse Gases Observing Satellite (GOSAT) products reveal similar
20 seasonal variation. The seasonal amplitude of the column-averaged CO₂ mole fractions is
21 smaller than that of the ground-based CO₂ at all stations. The extrema of the seasonal cycle of
22 ground-based and column CO₂ mole fractions are basically synchronous except a slight phase
23 delay at Lin’an (LAN) station. For the two-year average, the column CO₂ is lower than ground-
24 based CO₂, and both of them reveal the lowest CO₂ mole fraction at Waliguan (WLG) station.
25 The lowest (~4 ppm) and largest (~8 ppm) differences between the column and ground-based
26 CO₂ appear at WLG and Longfengshan (LFS) stations, respectively. The CO₂ mole fraction and
27 its difference between GOSAT and ground-based measurement are smaller in summer than in
28 winter. The differences of summer column CO₂ among these stations are also much smaller
29 than their ground-based counterparts. In winter, the maximum of ground-based CO₂ mole
30 fractions and the greatest difference between the two (ground-based and column) datasets

31 appear at the LFS station. Secondly, the representative areas of the monthly CO₂ background
32 mole fractions at each station were found by employing footprints and emissions. Smaller
33 representative areas appeared at Shangdianzi (SDZ) and LFS, whereas larger ones were seen at
34 WLG and LAN. The representative areas in summer are larger than those in winter at WLG
35 and SDZ, but the situation is opposite at LAN and LFS. The representative areas for the stations
36 are different in summer and winter, distributed in four typical regions. The CO₂ net fluxes in
37 these representative areas show obvious seasonal cycles with similar trends but different
38 varying ranges and different time of the strongest sink. The intensities and uncertainties of the
39 CO₂ fluxes are different at different stations in different months and source-sink sectors. Overall,
40 the WLG station is almost a carbon sink, but the other three stations present stronger carbon
41 sources for most of the year. These findings could be conducive to the application of multi-source
42 CO₂ data and the understanding of regional CO₂ source-sink characteristics and patterns over China.
43 *Keywords:* Atmospheric CO₂; Flask sampling observation; GOSAT; Source-sink characteristic;
44 Atmospheric background station

45

46 **1. Introduction**

47 CO₂ contributes more than 50% of the total climate forcing caused by long-lived greenhouse
48 gases, which is the primary driving factor of climatic changes involving surface temperature,
49 hydrological cycle, sea level rise, and extreme weather events (IPCC-AR5, 2013). The global
50 average tropospheric mole fraction of monthly CO₂ was approximately 404 parts per million
51 (ppm) in April 2016, and the rate of increase was at a record high during 2015 and 2016
52 (www.esrl.noaa.gov/gmd/ccgg/trends/). The anthropogenic CO₂ emissions from fossil-fuel
53 combustion and cement production amounted to approximately 9.1 PgC in 2010, and about 55%
54 of these emissions were absorbed by the terrestrial ecosystem and ocean (Ballantyne et al., 2012;
55 Peters et al., 2011). As unprecedented population growth and resource consumption have led to
56 highly increased CO₂ emissions since the early 1980s, it is significant to understand further the
57 patterns of atmospheric CO₂ mole fraction and source-sink characteristics over China through
58 multi-source and multi-site data (Piao et al., 2009; Zhang et al., 2014c).

59 The mole fraction of CO₂ is almost the same everywhere, but relatively small differences,
60 especially near the surface, are caused by recent emissions and removals (Zhang et al., 2013b).

61 The variation and source–sink characteristics of CO₂ over China have been investigated by
62 using observation data from different platforms and statistical data (Xu et al., 2017). In the
63 framework of the World Meteorological Organization’s Global Atmosphere Watch
64 (WMO/GAW), atmospheric greenhouse gases have been observed continuously at four
65 background stations in China (WLG: Waliguan, SDZ: Shangdianzi, LAN: Lin’an, LFS:
66 Longfengshan) (Fang et al., 2014; Liu et al., 2009; Zhou et al., 2006). The traceable, comparable,
67 and high-precision CO₂ data obtained at these stations have been used widely in many studies,
68 such as source–sink inversion studies (Jiang et al., 2013; Zhang et al., 2014a). Although the
69 variation of CO₂ mole fraction can be obtained accurately by the WMO/GAW network of
70 ground stations, this measurement with sparse spatial coverage is time consuming and easily
71 affected by surrounding environment (Liu et al., 2014). Satellite remote sensing has been used
72 to monitor CO₂ column mole fraction since 2002 because it has the advantages of spatial
73 coverage, speed, and continuity (Boesch et al., 2011; Buchwitz et al., 2004; Clerbaux et al.,
74 2009; Jiang et al., 2010; Kulawik et al., 2010; Tangborn et al., 2013; Xu et al., 2017; Yokota et
75 al., 2009; Zhang et al., 2015). However, satellite retrievals of CO₂ (and other greenhouse gases)
76 cannot be calibrated. They are only useable if systematic biases, many of which remain
77 unknown, can be reduced to extremely low levels, to less than 0.1 ppm in the case of CO₂ (Fang
78 et al., 2016; Masarie et al., 2001). Several detectors have been launched into space, including
79 the Atmospheric Infrared Sounder (AIRS), the Scanning Imaging Absorption Spectrometer for
80 Atmospheric Cartography (SCIAMACHY), the Greenhouse Gases Observing Satellite
81 (GOSAT), the second Orbiting Carbon Observatory (OCO-2), and the Chinese Carbon Dioxide
82 Observation Satellite (TanSat) (Aumann et al., 2003; Bovensmann et al., 1999; Chen et al.,
83 2017; Frankenberg et al., 2015; Kuze et al., 2009). The retrievals from these satellites need to
84 be compared to calibrated in-situ (at the surface and in the vertical column) measurements to
85 discover, and then eliminate, retrieval biases. Currently, atmospheric transport models are used
86 to combine the two types of data and study their level of compatibility, but this method has its
87 own limitations because transport model biases cause discrepancies in addition to those
88 between the two types of data (Baker et al., 2010; Chevallier et al., 2011; Chevallier et al., 2009;
89 Cogan et al., 2012; Houweling et al., 2004; Jiang et al., 2013; Lauvaux et al., 2009; Miller et
90 al., 2007; Nassar et al., 2011; Peters et al., 2007; Pillai et al., 2010; Reuter et al., 2011; Streets

91 et al., 2013; Zhang et al., 2014a). Here, we use satellite retrievals of atmospheric CO₂ over four
92 WMO/GAW stations in China to reveal the CO₂ pattern and assess the coherence of different
93 datasets (Zhou et al., 2013).

94 The pattern of CO₂ mole fraction at each station is highly correlated to the source and sink
95 characteristics of CO₂ in a specific area, which is called “source–sink regional
96 representativeness.” The key for this representativeness is to find the representative area, which
97 has been explored at the WLG station through simulation results (Cheng et al., 2017a). The
98 representative area and source–sink characteristics of this area are important for understanding
99 the regional differences of CO₂ mole fraction, evaluating the site layout, and developing
100 emission reduction strategies because of the differences in the stage of economic development
101 and the diverse climates in China (Xu et al., 2017). Some studies have focused on the
102 representativeness of fluxes, radiation, temperature, and air pollutants (e.g., Xu et al., 2015).
103 Researches on the patterns and sources of CO₂ mole fraction at the WMO/GAW stations in
104 China have also been conducted by using the method of isotope tracing and individual
105 trajectories (Xia et al., 2015; Zhang and Zhou, 2013). However, to the best of our knowledge,
106 there are no comparison studies on the representative areas of CO₂ background mole fractions
107 at the four WMO/GAW stations in China, as well as the source–sink characteristics in the
108 representative areas.

109 This study aims to examine the variation of CO₂ mole fractions using calibrated in-situ
110 sampling observations and the GOSAT retrieval products and compare the source–sink regional
111 representativeness of the CO₂ background mole fractions at China’s four WMO/GAW stations.
112 Section 2 introduces the sites, CO₂ sampling, GOSAT products, and the statistical analysis
113 methods for source–sink regional representativeness. Section 3 presents the results with
114 discussion and consists of two parts: (1) a comparison of CO₂ mole fraction between the surface
115 observations at the four WMO/GAW stations and the GOSAT products and (2) an evaluation
116 of the representative areas of CO₂ background mole fractions and a comparison of the source–
117 sink characteristics corresponding to the CO₂ background mole fractions at the four
118 WMO/GAW stations. Finally, the summary and conclusions are presented in Section 4.

119

120 **2. Data and Methods**

121 *2.1. Sites and CO₂ sampling observations*

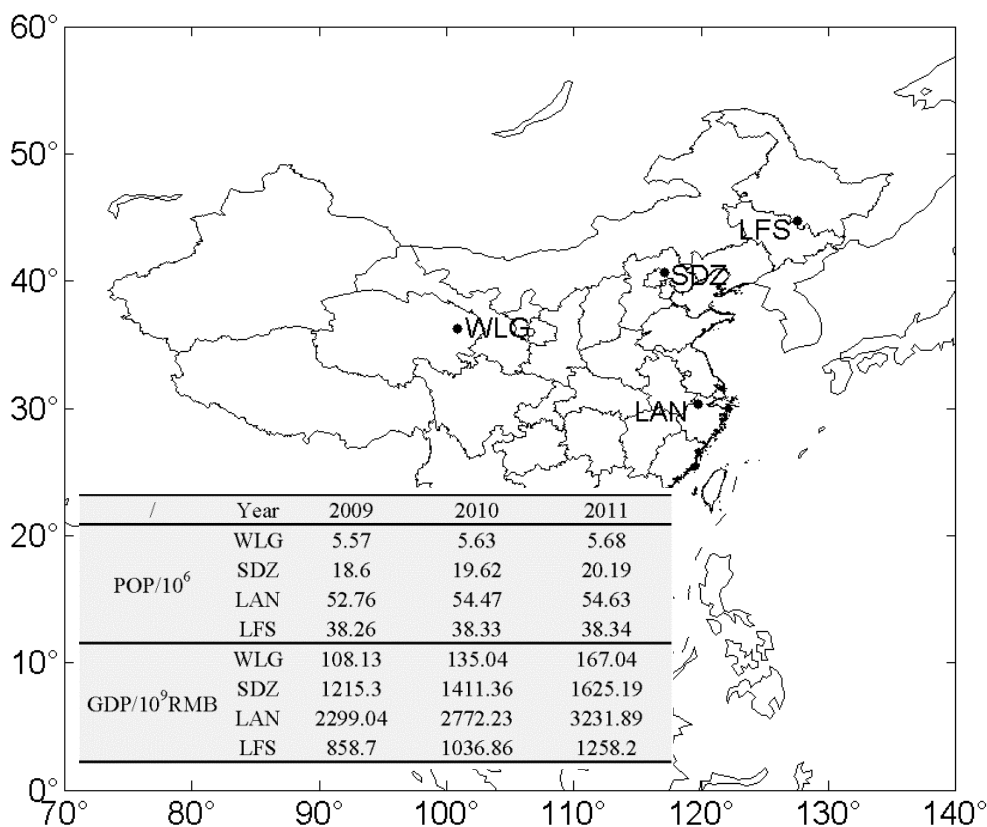
122 Atmospheric CO₂ samples were collected by flasks during 2009–2011 at the four stations of
123 the WMO/GAW network in China (Fig. 1). The population and gross domestic product
124 (<http://data.stats.gov.cn/>) of the provinces affiliated with these sites are also shown by the table
125 inserted into Fig. 1. These stations are global or regional background stations, representing
126 atmospheric conditions in different climate features, vegetation types, and economic zones in
127 China (Fang et al., 2014; Liu et al., 2009).

128 The WLG station (36°17' N, 100°54' E; 3810 m asl) is located on the northeastern edge of
129 the Tibetan Plateau (Liu et al., 2014). This station is isolated from industrial and population
130 centers. Yak and sheep grazing is the main economic activity in summer. The area surrounding
131 the WLG station has maintained its natural environment of arid/semi-arid grassland and desert
132 steppe and has a typical plateau continental climate with predominant wind directions of
133 southwest in winter and northeast/southeast in summer (Zhang et al., 2013a; Zhou et al., 2005).

134 The SDZ station (40°39' N, 117°07' E; 293 m asl) is about 120 km northeast of Beijing. The
135 area surrounding the SDZ station consists primarily of shrubs, orchards, and farmland. No large
136 industrial zone exists within 30 km of the station. The dominant wind directions are ENE in
137 autumn and winter and WSW in spring and summer (An et al., 2012).

138 The LAN station (30°18' N, 119°44' E; 138.6 m asl) lies on the top of a hill in Zhejiang
139 Province and is surrounded by forest, farming areas, and hilly land with a humid subtropical
140 monsoon climate. There are no large villages within 3 km of the station. The prevailing winds
141 there are northeasterly and southwesterly winds (Pu et al., 2014).

142 The LFS station (44°44' N, 127°36' E; 330.5 m asl) is located on the top of Mt. Longfengshan
143 in Heilongjiang Province. Agricultural areas lie to the north and west of LFS, and extensive
144 forested land exists to its east and south. No large cities or industrial zones exist within 40 km
145 of the station. LFS is dominated by a temperate continental monsoon climate (Liu et al., 2009).



146

147 **Fig. 1.** Geographical locations of the four WMO/GAW stations in China (black dots). The
 148 population (POP) and gross domestic product (GDP) in the affiliated provinces are shown in the
 149 inserted table.

150

151 At the four stations mentioned above, discrete surface CO₂ data from flask sampling and
 152 analysis have been obtained through the method recommended by WMO/GAW (Liu et al.,
 153 2014). To ensure the quality of the samplings, the flask is subjected to a 24 h vacuum test, filled
 154 with dry balance gas, flushed with local air, and then pressurized to ~6.5 psi above ambient
 155 pressure. Sampling begins in the morning (~8:00) local time at the WLJ station and in the
 156 afternoon (~14:00) at the other three regional stations when atmospheric conditions are suitable
 157 for capturing “background” characteristics (Liu et al., 2009). Air samples, collected
 158 approximately weekly, are transported to the Greenhouse Gases Research Laboratory of the
 159 China Meteorological Administration (CMA) for analysis. Generally, the CO₂ mole fractions
 160 are determined by a cavity ring down spectroscopy system (a non-dispersive infrared
 161 spectroscopy observation system before October 2009). The CO₂ values are calibrated by the
 162 reference gas and working high and low standard gases, which are traceable to the WMO X2007

163 standard scale. Due to sampling, storage, or measurement problems, CO₂ selection is an
164 important part of the data post-processing, such as for quality control, screening, and curve-
165 fitting. Partially because of its simplicity, the CO₂ dataset from flask sampling is reliable and
166 internationally comparable with high precision (Fang et al., 2015a; Li et al., 2014; Masarie et
167 al., 2001; Tans et al., 1989; Xia et al., 2015; Zhou et al., 2003).

168

169 2.2. GOSAT products

170 Designed specifically to retrieve the mole fractions of greenhouse gases (e.g., CO₂), the
171 Greenhouse Gases Observing Satellite (GOSAT) was launched to sun-synchronous orbit in
172 2009. It observes a same place every three recurrent days. Column-averaged CO₂ dry air mole
173 fraction can be retrieved from the shortwave infrared bands recorded by the sensor of the
174 Fourier transform spectrometer (FTS) onboard GOSAT (Miao et al., 2013). The optimal
175 estimation retrieval algorithm is used to obtain GOSAT Level 2 (L2) products (O'Dell et al.,
176 2012; Yoshida et al., 2011), estimating column-averaged CO₂ over a specific observation point
177 and at a specific time. The GOSAT Level 3 (L3) products, providing a monthly global
178 distribution of column CO₂ (2.5 × 2.5 degrees of grid as a unit), are generated by applying
179 statistical processing to the FTS L2 products. The data products (V02.xx) derived from GOSAT
180 observations have approximately a 2 ppm standard deviation when compared with ground-
181 based observations and in situ airborne measurement data (Lei et al., 2014). The GOSAT L2/L3
182 data products (V02.21), available at http://data2.gosat.nies.go.jp/index_en.html, were used in
183 this study.

184

185 2.3. Source–sink regional representativeness analysis

186 For the CO₂ background mole fractions at monthly scale at the four WMO/GAW stations in
187 China, a statistical method was used to explore their source–sink regional representativeness.
188 The key to the method is to determine the area where maximum correlation exists between time
189 series of atmospheric CO₂ mole fractions and regional emissions. The representative source–
190 sink regions can be found through simulations of the FLEXible PARTicle dispersion model
191 (FLEXPART) and the Carbon Tracker 2015 model (CT2015). The method is carried out in
192 following steps.

193 Firstly, an emission sensitivity function or transport climatology is calculated by 3-hourly
 194 backward simulation of FLEXPART (Stohl et al., 2005). As most emissions appear in the layer
 195 adjacent to the surface, the emission sensitivity function in this layer is of particular interest
 196 and is here abbreviated as “Footprint,” which is determined by the particle residence time in
 197 grid cell and denotes the influence of the potential source on the observation site. Footprint
 198 $s(m)$ with $1^\circ \times 1^\circ$ horizontal resolution, corresponding to the m^{th} CO₂ mole fraction, can
 199 be calculated by releasing 50,000 particles at the observation site during the 3-hourly interval
 200 and following them backward for 7 days. There is a one-to-one correspondence between
 201 footprints and CO₂ mole fractions. If the number of selected CO₂ data in one month is M , the
 202 monthly footprint $s_{mon}(i, j)$ in a particular surface grid cell (i, j) is calculated as

$$203 \quad s_{mon}(i, j) = \sum_{m=1}^M s(i, j, m) \quad (1)$$

204 where $s_{mon}(i, j)$ represents the frequency of air masses in grid cell (i, j) arriving at the
 205 observation site. Based on the variable $s_{mon}(i, j)$, we assume a threshold value (T_r) of
 206 footprint and define a logic matrix $L_{mon}(i, j)$ as the mask grid.

$$207 \quad L_{mon}(i, j) = \begin{cases} 1 & s_{mon}(i, j) \geq T_r \\ 0 & s_{mon}(i, j) < T_r \end{cases} \quad (2)$$

208 Secondly, the spatial and temporal distributions of gridded CO₂ fluxes and mole fractions
 209 can be retrieved by the CT2015 model using the “top-down” method (Peters et al., 2007). The
 210 Carbon Tracker (CT) model, updated approximately once a year, is a CO₂ measurement and
 211 modeling system that tracks CO₂ emissions to the atmosphere (sources) and removals from the
 212 atmosphere (sinks) around the world (<http://www.esrl.noaa.gov/gmd/ccgg/carbontracker/>). The
 213 sources and sinks of CO₂ consist of four sectors in CT2015: land biosphere (“bio”), wildfire
 214 (“fires”), fossil fuel emissions (“ff”), and ocean (“ocean”). At a specific time and place, the
 215 simulated CO₂ mole fraction (c) is contributed by the initial well-mixed CO₂ mole fraction
 216 and the transport of fluxes from all global regions for a past period of time (Jiang et al., 2013;
 217 Zhang et al., 2014a). According to the time of selected CO₂ values, the monthly net fluxes
 218 $F_{mon}(i, j)$ [mol/(m²·s)] in each grid cell can be extracted from the CT2015 model. Both L_{mon}

219 and F_{mon} are global 180×360 grids/matrices (latitude \times longitude). Hence, monthly regional
 220 emissions can be calculated as

$$221 \quad E_{area} = \sum_{i=1}^{180} \sum_{j=1}^{360} a(i, j) F_{mon}(i, j) L_{mon}(i, j) \quad (3)$$

222 where $a(i, j)$ is the area of the $(i, j)^{th}$ grid.

223 Finally, the correlation coefficient (r) of the time series of regional emissions (E_{area}) and
 224 CO₂ mole fractions (c) at each station on a monthly scale can be calculated iteratively on the
 225 basis of different threshold values of footprint. As a result, the best footprint threshold value
 226 (T_R) and the maximum correlation (R) can be found through correlation analysis and
 227 numerical iteration. The representative source–sink region is confined by the best footprint
 228 threshold value as follows:

$$229 \quad L_{mon, T_R}(i, j) = L_{mon}(i, j) \quad (T_r = T_R) \quad (4)$$

230 which shows the area where emissions have the greatest influence on the atmospheric CO₂ mole
 231 fractions in a particular month for a specific observation station. The area of the representative
 232 source–sink region is:

$$233 \quad A = \sum_{i=1}^{180} \sum_{j=1}^{360} a(i, j) L_{mon, T_R}(i, j) \quad (5)$$

234 Based on the emission and the area of the representative source–sink region, regional fluxes
 235 F_{area} can be estimated:

$$236 \quad F_{area} = E_{area} / A \quad (6)$$

237 The different sectors (k) of source and sink in the representative source–sink region
 238 [$F_{mon, k, T_R}(i, j)$] can also be obtained by:

$$239 \quad F_{mon, k, T_R}(i, j) = F_{mon, k}(i, j) L_{mon, T_R}(i, j) \quad (7)$$

240

241 3. Results and discussion

242 3.1. Contrast analysis of CO₂ sampling observation and GOSAT product

243 3.1.1. Comparison of GOSAT L2 product with CO₂ mole fraction derived from the four

244 *WMO/GAW stations in China*

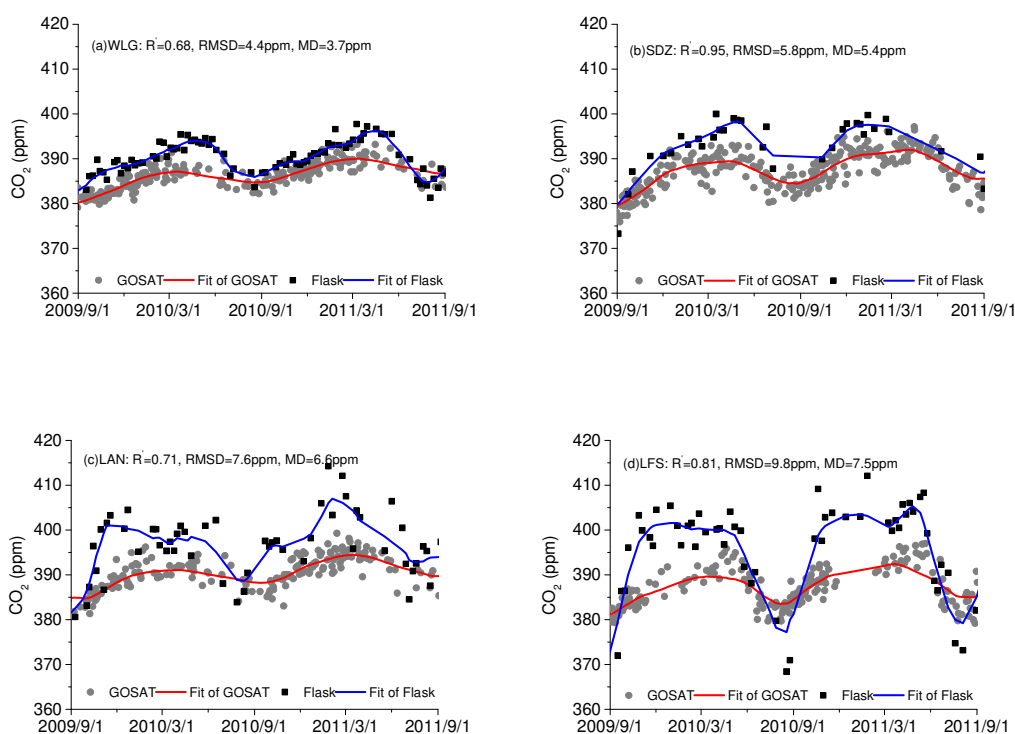
245 Fig.2 shows the qualified CO₂ mole fractions from September 2009 to August 2011 at the
246 WLG, SDZ, LAN, and LFS stations in China, separately obtained from flask sampling and
247 GOSAT L2 products. If more than one data point is available at a given station in a day, it is
248 averaged. The GOSAT data were selected when horizontal distance between a given station and
249 the geographic location of a GOSAT measurement was less than 500 km. Relatively, fewer
250 GOSAT CO₂ data can be collected at LAN in summer and at LFS in winter, which may be
251 attributed to the influence of the cloud, the locations of the two stations, and data selection
252 procedures of GOSAT. GOSAT does not work for high latitudes in winter, because FTS SWIR
253 (ShortWave InfraRed) requires sunlight with the Sun sufficiently high above the horizon (Bréon
254 and Ciais, 2010). In order to decrease the uncertainty of a single measurement, the CO₂ mole
255 fractions were smoothed by the curve-fitting method of Thoning et al. (1989) (Fig. 2).

256 The two datasets, from flask sampling and GOSAT, presented similar patterns of seasonal
257 variation at all four stations. The correlation coefficient R' ranges from 0.68 (WLG site) to 0.95
258 (SDZ site). The minimum CO₂ mole fraction appears in late summer and the maximum occurs
259 in spring or winter. Seasonal variations of atmospheric CO₂ at the four WMO/GAW stations
260 are dominated mainly by the exchange with the land biosphere. The occurrence time of the
261 seasonal CO₂ maximum is related to human activities, different regional terrestrial ecosystems,
262 and local meteorological conditions (Fang et al., 2014).

263 The mean differences (MD=3.7~7.5ppm) are positive at the four stations, probably because
264 the two datasets separately provide CO₂ dry air mole fractions at the surface and estimates of
265 the CO₂ column-averaged dry air mole fractions. The column-averaged CO₂ mole fractions are
266 manifest in the lower amplitude of the seasonal cycle which is produced at the surface and
267 attenuated at higher altitudes (Jiang et al., 2016). A slight phase delay can also be expected, but
268 this is not very clear except at LAN station from Fig. 2. It can be further identified by the fact
269 that the ground-based CO₂ is significantly less than the column CO₂ in summer because of the
270 strong uptake by rice plants and forests at LFS.

271 There are some differences in CO₂ mole fractions among these stations. For ground-based
272 CO₂, the seasonal amplitudes (peak-to-peak value) range in a diminishing sequence from LFS,
273 SDZ, LAN, to WLG. Differing from the regional background stations of LAN and LFS, the

274 maximum of CO₂ mole fractions at WLG is low, which may be due to the site's high altitude
 275 and its location far from industrial zones and large cities (Liu et al., 2009). The biggest R'=0.95
 276 and RMSD=9.8ppm appear at SDZ and LFS stations, respectively. WLG station presents the
 277 smallest values of R'=0.68, RMSD=4.4ppm, and MD=3.7ppm. So, generally speaking, the
 278 characteristics of GOSAT column CO₂ are similar to the ground-based CO₂, but the differences
 279 of the seasonal amplitudes and levels of GOSAT column CO₂ among these stations are smaller.



280

281

282 **Fig. 2.** Comparison of CO₂ mole fraction between flask sampling observation (black squares) and
 283 GOSAT L2 product (gray dots) at China's four WMO/GAW stations. Blue and red lines are fitting
 284 curves. R', RMSD, and MD denote the correlation coefficient, root mean square difference, and
 285 mean difference (Flask minus GOSAT), respectively, between the fitting CO₂ mole fractions of the
 286 two datasets.

287

288 3.1.2. Spatial distribution of atmospheric CO₂ mole fractions

289 There is a higher spatial coverage for the current GOSAT CO₂ measurement, although the
 290 accuracy and precision of GOSAT CO₂ mole fraction are lower than those of the surface flask
 291 sampling observation. The spatial distributions of column CO₂ over China in summer and
 292 winter as well as in the two years (September 2009–August 2011) were extracted from the
 293 GOSAT L3 products (Fig. 3). The whitened portions in the figure represent places where data
 294 do not exist within the range of 500 km from the processed points. The difference of the GOSAT

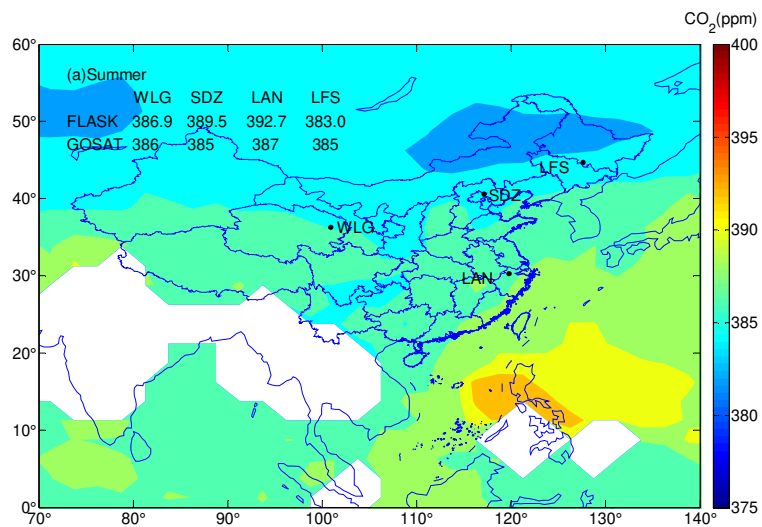
295 column CO₂ spatial distribution is significant over China, with low mole fractions in summer
296 and high mole fractions in winter. In summer, higher CO₂ mole fractions are concentrated
297 mainly in the southern and eastern coastal regions of China, while lower values are distributed
298 in Inner Mongolia and Northeast China. However, column CO₂ is higher in most parts of China
299 in winter, except for Qinghai and parts of Tibet, Gansu, and Inner Mongolia. From the two-year
300 average (Fig. 3c), the column CO₂ distribution presents a significant spatial gradient from east
301 to west, with CO₂ mole fractions distributing from high to low, respectively. This pattern is
302 consistent with the result retrieved from SCIAMACHY, and the seasonal differences may be
303 connected with regional Normalized Difference Vegetation Index (NDVI) and air temperature
304 (Wang et al., 2015).

305 The mean CO₂ mole fractions from the sampling measurement at the four WMO/GAW
306 stations and the matched grids (2.5° × 2.5°) of GOSAT L3 product are also shown by the
307 overlain tables, respectively (Fig. 3). For the two-year average (Fig. 3c), full column CO₂ is
308 lower than CO₂ mole fraction adjacent to the surface, but the difference between them remained
309 approximately within the region of 4–8 ppm at these WMO/GAW stations. The CO₂ mole
310 fraction at the WLG station is the lowest among the four stations, whether for flask sampling
311 or for GOSAT retrievals. The largest differences (~8 ppm) of CO₂ mole fraction between flask
312 data with GOSAT appear at LFS station.

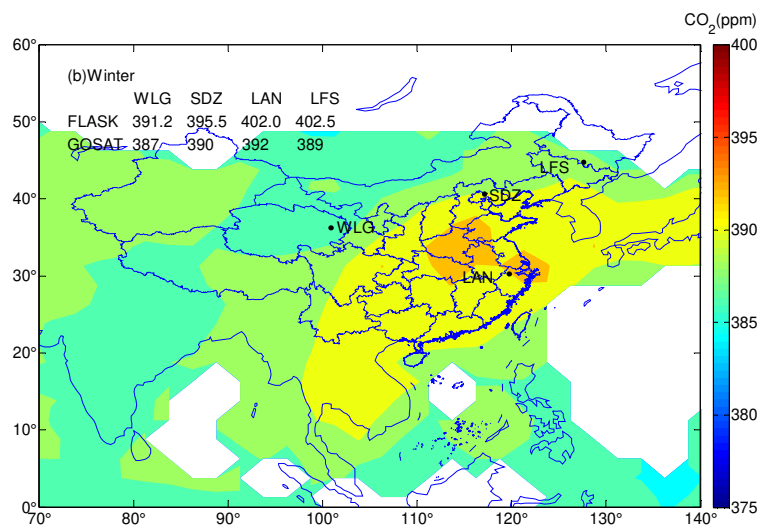
313 In summer (Fig. 3a), full column CO₂ is lower than CO₂ mole fraction observed by flask
314 sampling at all stations except LFS. Compared with the values in winter or the two-year average,
315 the CO₂ mole fraction and its difference between full column and surface are smaller in summer.
316 The maximum and minimum CO₂ mole fraction in the two datasets occur at LAN and LFS,
317 respectively, but the differences of full column CO₂ at these stations are much smaller than
318 those of their surface counterpart. In winter (Fig. 3b), full column CO₂ is lower than ground-
319 based CO₂. The maximum of ground-based CO₂ mole fractions and the largest difference
320 between the two datasets appear at the LFS station, perhaps due to heating in Northeast China.

321 Overall, we estimate that there may be stronger anthropogenic emissions at the SDZ and
322 LAN stations and weaker sinks at the WLG station, i.e., weaker sources at the WLG and LFS
323 stations but stronger sinks at the SDZ, LAN and LFS stations. The estimation of stronger
324 terrestrial CO₂ sinks at regional background stations can be confirmed by the distribution of

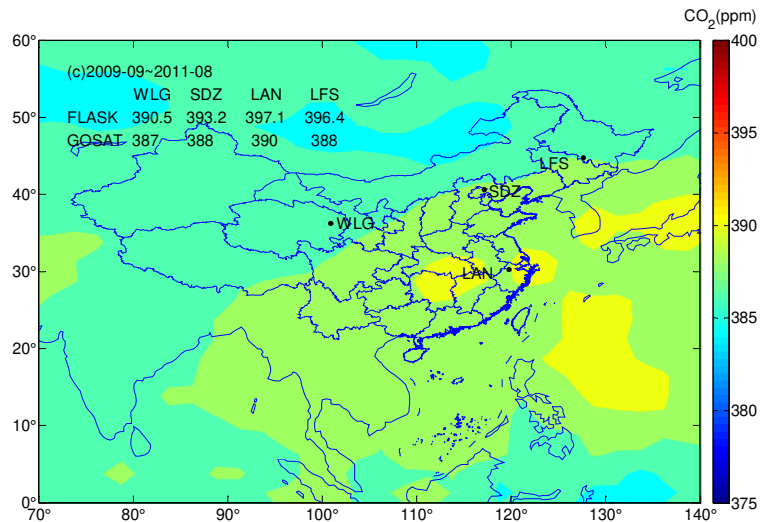
325 gross primary production (Sun et al., 2018). This is also consistent with previous studies in the
326 southeast and northeast China (Liu et al., 2012; Zhang et al., 2014b).



327



328



329

330 **Fig. 3.** Spatial distribution of CO₂ mole fractions from GOSAT L3 products (a) in summer (June,
 331 July, August) and (b) in winter (December, January, February) and (c) in September 2009–August
 332 2011. Black dots denote the four WMO/GAW stations. Overlain tables show the mean CO₂ mole
 333 fractions from flask sampling at these stations and the matching grid cells of GOSAT retrievals.

334

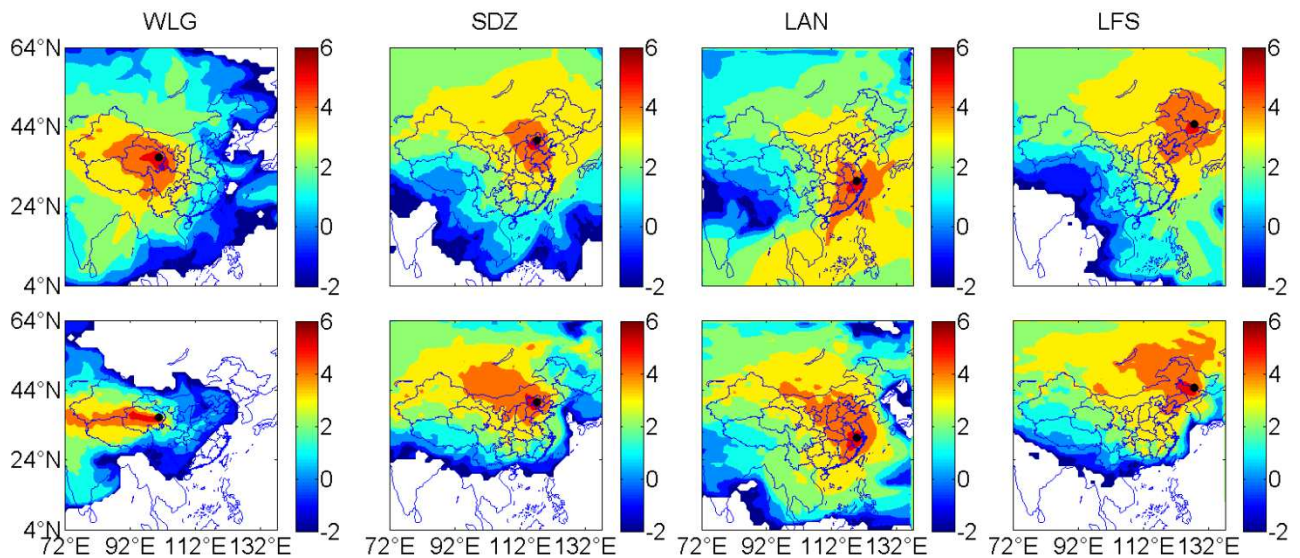
335 3.2. Source–sink regional representativeness

336 The spatial and temporal patterns of atmospheric CO₂ mole fractions are closely related to
 337 CO₂ source and sink as well as the transport of the atmosphere. Based on the steps of the
 338 statistical method introduced in Section 2.3 and the simulations of FLEXPART and CT2015,
 339 the source–sink regional representativeness of the atmospheric CO₂ background mole fractions
 340 at the four WMO/GAW stations in China were compared.

341 3.2.1. Footprint

342 The footprints for summer and winter at the four WMO/GAW stations indicate the sensitivity
 343 to surface emissions during the transport of the previous 7 days (Fig. 4). The description “7
 344 days” is a compromise between the enough large spatial coverage and the calculation time of
 345 footprint simulation (An et al., 2014). An emission area with a higher footprint value has a
 346 larger impact on the observation site. There are pronounced differences between summer and
 347 winter footprints for all four sites, which are closely related to the seasonal transition of air
 348 mass transport over China. Due to the influence of summer monsoon, the high footprint values
 349 (>4) at WLJ in summer are distributed mainly in western China, although air masses from
 350 Southeast Asia and the Bay of Bengal play a role in the atmospheric CO₂ mole fraction (Xu et
 351 al., 2013). The high footprint values (>4) in winter are concentrated to the west of the WLJ

352 station, which is a consequence of the dominant westerlies and consistent with atmospheric
 353 transport patterns for a large area of western China (Li et al., 2014). At the SDZ station, the
 354 high footprint values (>4) are distributed mainly in its southeast and northwest in summer and
 355 in its northwest in winter, which is probably associated with the Pacific Subtropical High in
 356 summer and the Siberian High in winter, respectively. The distribution of high footprint values
 357 (>4) at LAN in summer is related to clean air masses from the sea, but relatively colder air masses
 358 containing CO₂ emitted in the east of China are prone to reach the LAN station in 7 days in winter
 359 (Cheng et al., 2017b). The high footprint values (>4) at LFS in summer, with a distribution
 360 similar to that at the LAN station, are distributed mainly in Northeast China, northeastern Inner
 361 Mongolia, and the Sea of Japan, but the high values (>4) in winter are primarily limited to the
 362 northwest of the LFS station. The footprint distributions at three regional stations (SDZ, LAN, and
 363 LFS) are similar to some degree in winter because of the effect of northwesterly air flows. Therefore,
 364 along with the atmospheric circulation switching between seasons, there are different potential
 365 source areas for the four WMO/GAW stations (An et al., 2014; Lu et al., 2012).



366

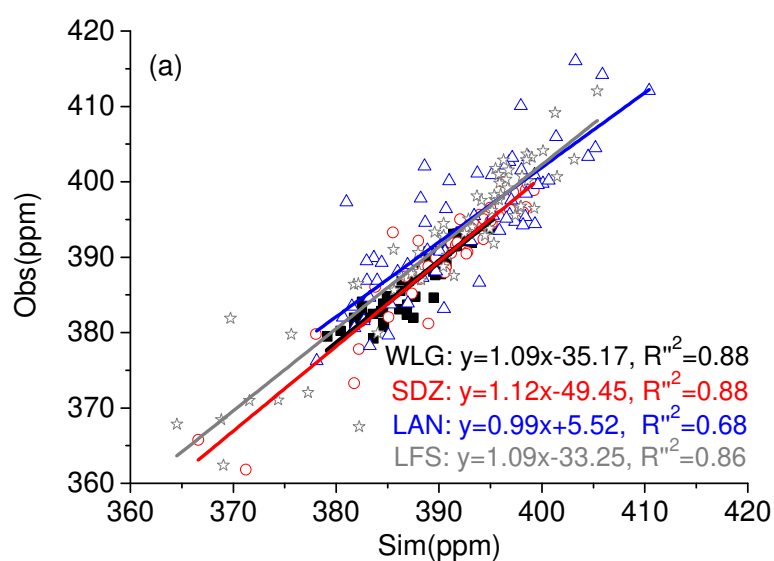
367 **Fig. 4.** Footprint distributions in logarithmic units ($\log_{10}s$) for summer (top row) and winter (bottom
 368 row) of 2009 at the WMO/GAW stations. Black dot represents the location of station.

369

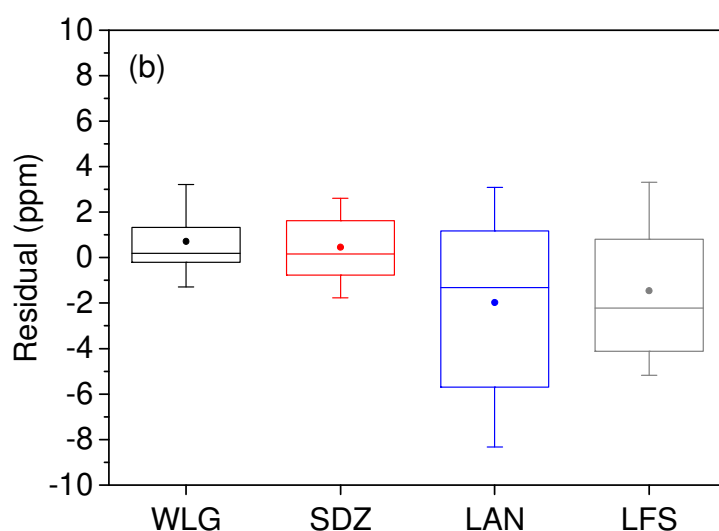
370 3.2.2. Data verification and screening

371 Before the CO₂ background extraction from CT2015 simulation results, the results were
 372 compared with surface observation values at the four WMO/GAW stations. We used the
 373 simulated CO₂ mole fractions with a $3^\circ \times 2^\circ$ horizontal grid for a 3-hour interval in the vertical

374 layer adjacent to the surface. Outliers in simulation appear because of the “model data mismatch”
375 (MDM), which can be described in different ways and partly defines the rejection criterion
376 (Zhang et al., 2014a; Zhang et al., 2014b). In the post-processing of the CO₂ simulation data,
377 we eliminated outliers when the simulation results exceeded the range of monthly observed
378 average CO₂ mole fraction ± 3 times the standard error of the monthly mean. We selected the
379 qualified CO₂ simulation results and matched them with the sampling observations within 1.5
380 h in the grid cells of each station. Fig. 5a shows the linear regression analysis of atmospheric
381 CO₂ mole fractions between observation and simulation at the four WMO/GAW stations from
382 March 2008 to February 2011. The correlation coefficient R'^2 at each station ranges from 0.68
383 (LAN site) to 0.88 (WLG and SDZ sites). The slope of the linear fitting is close to 1 for all
384 stations. Fig.5b presents the residuals (simulation minus observation) of CO₂ mole fractions at
385 each station. The fluctuations of the residual are smaller at WLG and SDZ stations than at the
386 other two stations from the aspect of the 10th (90th) and the 25th (75th) percentiles. The median
387 and mean values of residuals are less than 2ppm at the four WMO/GAW stations. The bigger
388 deviations mostly appear in the highest and lowest CO₂ mole fractions between observations
389 and simulations. In spite of this, previous studies showed that there are no significant
390 differences in capturing the background variation at these stations as a whole through the low-
391 resolution (3°×2°) and high-resolution (1°×1°) simulations (Cheng et al., 2013). So it is possible
392 that the patterns of atmospheric CO₂ background mole fraction near the surface can be extracted
393 from the CT2015 results.



394



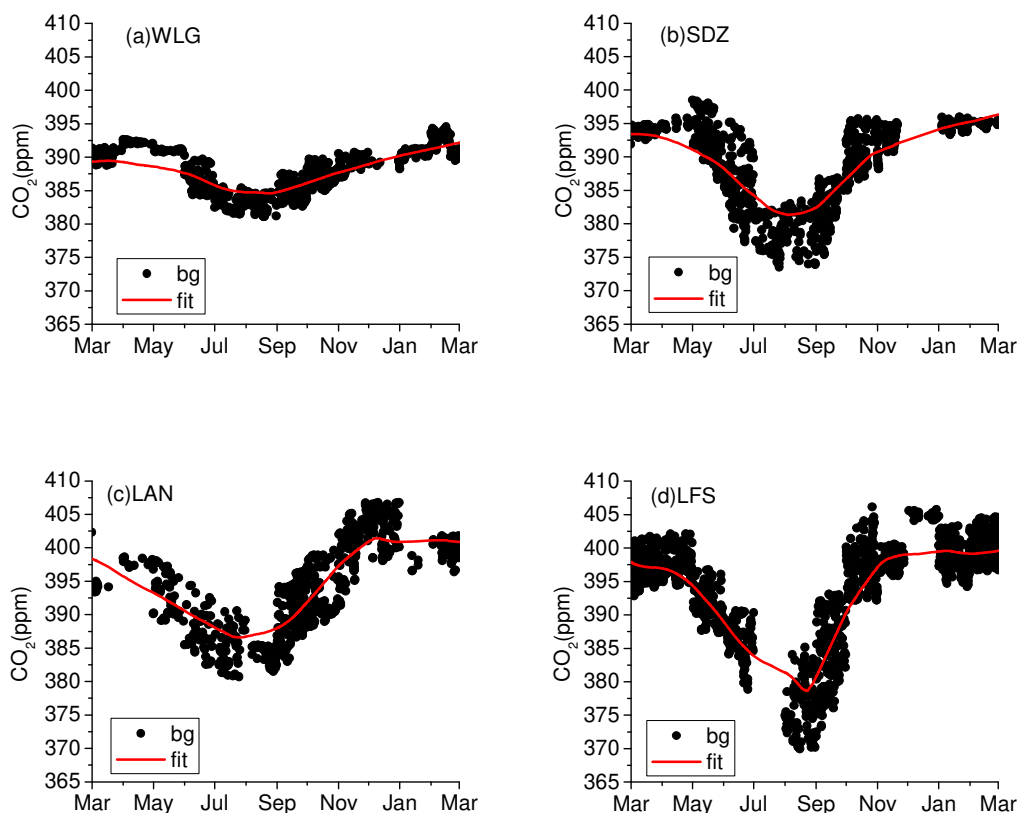
395

396 **Fig. 5.** Comparison of CO₂ mole fractions between single flask sampling observation and CT2015
 397 simulation from March 2008 to February 2011: (a) linear regression analysis of CO₂ mole fractions
 398 at WLG (black), SDZ (red), LAN (blue), and LFS (gray); (b) Lower (upper) error bars, boxes,
 399 hyphens inside the boxes, and circles are the 10th (90th), 25th (75th) percentiles, the medians, and
 400 the mean values of the residuals (simulation minus observation) of CO₂ mole fractions at each
 401 station, respectively.

402

403 The atmospheric CO₂ background mole fractions at a specific station reflect the regional
 404 atmospheric conditions, which can be obtained from the qualified CO₂ simulation results above.
 405 There are many different approaches for filtering time series of CO₂ data (Fang et al., 2015b).
 406 With the statistical extraction method of Robust Extraction of Background Signal (REBS), the

407 qualified time series of simulated CO₂ mole fractions can be screened into background and non-
408 background (Ruckstuhl et al., 2012). We selected the CO₂ background mole fractions from
409 March 2009 to February 2010 (Fig. 6), which were smoothed by the curve-fitting method of
410 Thoning et al. (1989). The bandwidth was set to 60 days in the algorithm of REBS until the
411 differences between CO₂ background mole fractions and fitted values were within 2 times the
412 standard deviation of the CO₂ simulation background. However, the seasonal CO₂ background
413 trends at the four WMO/GAW stations could be well captured by the “fitting curve”. For
414 example, the maximum and minimum seasonal fluctuations appear at the LFS and WLG
415 stations, respectively, matching the observation. The minimum of CO₂ mole fractions occurs
416 about in August because of stronger photosynthesis of plants in the growing season, and the
417 maximum occurs in spring or winter (Li et al., 2017). The monthly average of the fitted results
418 is used as specific time series to study the source–sink regional representativeness of CO₂
419 background mole fractions at the four WMO/GAW stations in the following.



422 **Fig. 6.** Simulated CO₂ background mole fractions (“bg”) and fitting curves (“fit”) obtained by
423 screening the qualified CT2015 data at the WMO/GAW stations.

424

425 3.2.3. Representative area

426 According to the method of source–sink regional representativeness, we obtained the areas
427 where the source and sink have the greatest impact on the monthly CO₂ fitted background mole
428 fractions at the four WMO/GAW stations. In the process of statistical analysis, we used the
429 monthly average data of 1° × 1° footprints from FLEXPART and 1° × 1° fluxes from CT2015
430 during the period from March 2009 to February 2010. The representative source–sink area was
431 estimated through the best footprint threshold value. After a series of iterative calculations and
432 correlation analysis, the best footprint threshold values (T_R) and the maximum correlation
433 coefficients (R) were separately determined at the four WMO/GAW stations, as shown in Table
434 1. The area (A) of the best threshold region, where there is maximum correlation between
435 regional CO₂ emissions and atmospheric CO₂ background mole fractions at each station on a
436 monthly scale, was calculated by Eq. 5. The maximum correlation coefficients ranged from
437 0.73 (WLG) to 0.94 (LFS). The larger of the best footprint threshold values appeared at the
438 SDZ and LFS stations, corresponding to the smaller areas of the best threshold region. At WLG
439 and LAN, the time series of atmospheric CO₂ background mole fractions represented larger
440 space with the smaller of the best footprint threshold values.

441 The areas of the best threshold region in summer and in winter are also presented in Table 1.
442 The source–sink regional representativeness of atmospheric CO₂ background mole fractions,
443 i.e., the best threshold area, changes with the seasons at a specific site, depending on the
444 variation of atmospheric circulations. The representative areas are larger in summer than in
445 winter at the WLG and SDZ stations, but the situations are opposite at the LAN and LFS stations.
446 There are larger differences of best threshold area between summer and winter at the WLG (6.3
447 × 10⁵ km²) and LAN (−9.1 × 10⁵ km²) stations. The maximum and minimum source–sink
448 regional representativeness occur at the WLG and LFS stations in summer, respectively, but
449 separately appear at the LAN and SDZ stations in winter. Due to different attributions, the
450 extrema of representativeness and atmospheric CO₂ background mole fraction are not always
451 synchronous. According to the differences of the best footprint threshold values, the
452 distributions of best threshold area are significantly different whether in summer or winter or
453 among different stations. To the best of our knowledge, no researches directly compare the

454 representative areas at these stations, but the results above are qualitatively comparable with
 455 back-trajectory analyses of the source of CO₂ (An et al., 2012; Fang et al., 2015a; Fang et al.,
 456 2015b; Zhang and Zhou, 2013). On the whole, the monthly atmospheric CO₂ background mole
 457 fractions from March 2009 to February 2010 at the four WMO/GAW stations mainly reflect
 458 variations of the sources and sinks in the best threshold area. Although the best threshold areas
 459 cover many regions in China, additional observation sites are needed to evaluate the CO₂
 460 condition.

461

462 **Table 1.** Source–sink regional representativeness for the monthly CO₂ fitted background mole
 463 fractions from CT2015 at the WMO/GAW stations.

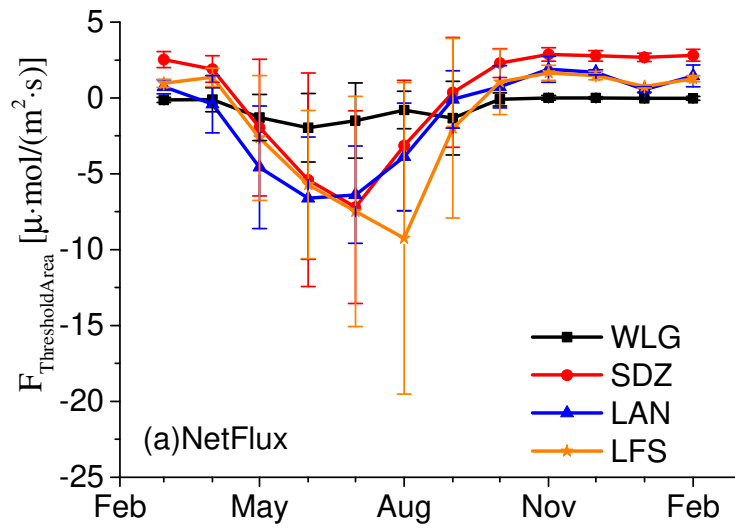
Representativeness	R	T_R (log ₁₀ S)	A (10 ⁶ km ²)	
			summer	winter
WLG	0.73	1.5	2.160	1.530
SDZ	0.78	2.8	0.180	0.123
LAN	0.87	1.6	2.070	2.980
LFS	0.94	2.4	0.135	0.389

464

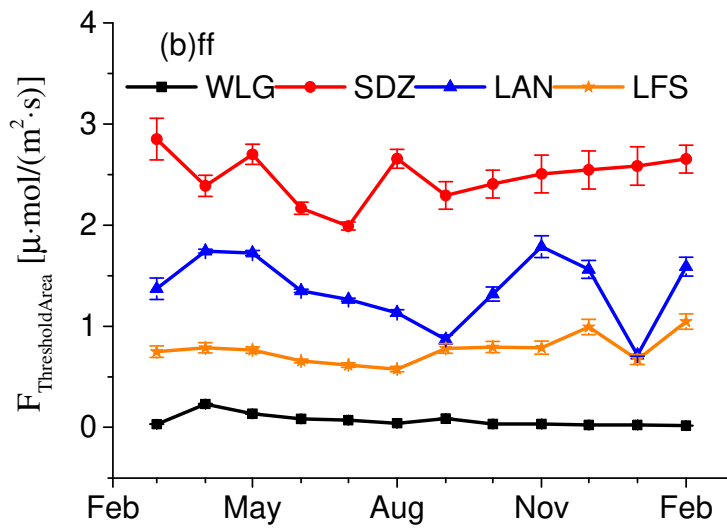
465 3.2.4. Source and sink in representative region

466 Fig. 7a shows the monthly averages and standard deviations of CO₂ fluxes from March 2009
 467 to February 2010 in the best threshold area, closely associated with the sources and sinks of
 468 atmospheric CO₂ background mole fractions at the four WMO/GAW stations in China. There
 469 are obvious seasonal cycles with similar trends among these stations for CO₂ fluxes. The
 470 fluctuation feature of the CO₂ flux at the WLG station in August is probably a result of air mass
 471 from the higher emission regions in China. There are greater uncertainties of the CO₂ fluxes for
 472 these stations between May and September, perhaps partly due to the low-resolution simulation.
 473 Overall, WLG is almost a carbon sink in representative area, but the other three regional stations
 474 are stronger carbon sources for most of the year from the perspective of fluxes. The uncertainty
 475 of the CO₂ fluxes is less in representative area of WLG station than that at the other three
 476 stations. The strongest and weakest carbon sinks occur at the LFS and WLG stations,
 477 respectively. Some differences are found in the time of the strongest carbon sink at the different
 478 stations, which is possibly due to the differences of vegetation and growing season.

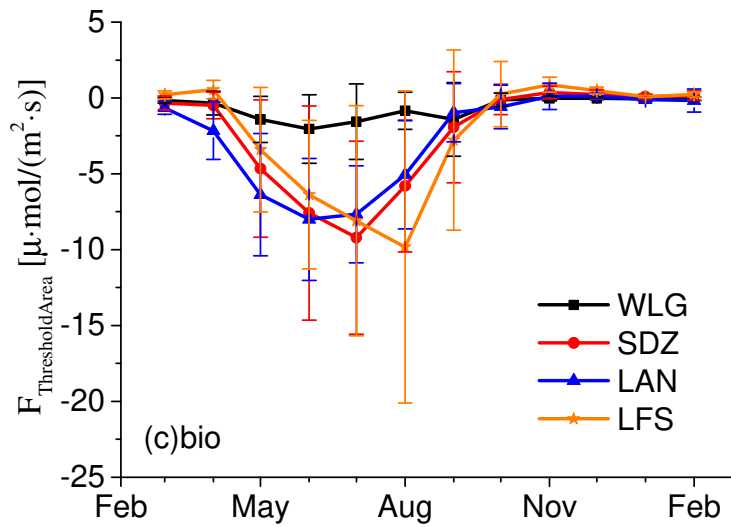
479 Additional details can be found by examining the monthly source and sink sectors (“fires,”
480 “ff,” “bio,” and “ocean”) in the best threshold area of the four WMO/GAW stations. The
481 contributions of “fires” and “ocean” (not shown in Fig.7) to the atmospheric CO₂ background
482 mole fractions are nearly negligible at each station compared to the influences of fossil fuel
483 burning (“ff”, Fig.7b) and terrestrial biosphere (“bio”, Fig.7c). The seasonal variation of CO₂
484 background mole fraction is controlled mainly by “bio,” although there are some seasonal
485 differences in “ff.” The “bio” acts mainly as a carbon sink for these stations between May and
486 September. The monthly variations of the “ff” fluxes are larger at SDZ and LAN stations than
487 at the other two stations, which are probably caused by the relatively high regional emissions
488 and sometimes by the air mass from the relatively clean areas, respectively. Compared with the
489 uncertainty of the “ff” flux, the uncertainty of the “bio” flux is larger, playing the dominant role
490 in the uncertainty of the net CO₂ flux, especially in the month of the stronger carbon sink. As
491 typical stations, the four stations have very different CO₂ source and sink characteristics (Liu
492 et al., 2015). Among the four stations, the bigger uncertainties of the “ff” and “bio” fluxes
493 appear at SDZ and LFS stations, respectively. The intensities of CO₂ source and sink are the
494 weakest at WLG as the consequence of less human activity and semi-arid grassland vegetation.
495 The strongest CO₂ source of 2.85 μ•mol/(m².s) with stronger CO₂ sink appear at SDZ, probably
496 because of the Beijing–Tianjin–Hebei economic circle of North China and the shrub vegetation.
497 The CO₂ source and sink at LAN are strong, possibly due to the Yangtze River Delta Economic
498 Zone and the hilly lands. The strongest CO₂ sink of –9.83 μ•mol/(m².s) appears at LFS with
499 weaker source, which might be generated by the forest vegetation and the northeast old
500 industrial base in China. These discrepancies and similarities among the stations indicate that
501 the atmospheric CO₂ background mole fractions at the four WMO/GAW stations can play a
502 significant role in understanding regional source–sink characteristics, although it is necessary
503 to reduce the uncertainty of CO₂ source and sink in the best threshold region in future’s studies.



504



505



506

507 **Fig. 7.** Monthly means and standard deviations of CO₂ fluxes from March 2009 to February 2010
 508 in the best threshold area for the four WMO/GAW stations: (a) net fluxes, (b) major source (“ff”),
 509 and (c) major sink (“bio”). “ThresholdArea” denotes the best threshold area. “F” denotes fluxes.
 510

511 4. Conclusions

512 This study compared the atmospheric CO₂ mole fractions between surface measurement and
 513 satellite retrieval at four WMO/GAW stations in China and found the representative areas of
 514 the atmospheric CO₂ background mole fractions for each station through a statistical method.
 515 Additionally, the source and sink in the representative areas were compared. The main findings
 516 are summarized below.

517 The CO₂ mole fractions from flask sampling and GOSAT L2 products present similar
 518 seasonal patterns at each station from September 2009 to August 2011. For ground-based CO₂,
 519 the seasonal amplitude (peak-to-peak value) varies in a diminishing sequence from LFS, SDZ,
 520 LAN, to WLG. The column-averaged CO₂ mole fractions are manifest in the lower amplitude
 521 of the seasonal cycle. The extrema of the seasonal CO₂ mole fractions from the two datasets
 522 are basically synchronous for the specific stations, except a slight phase delay at LAN station.
 523 The biggest correlation coefficient ($R'=0.95$) and the root mean square difference
 524 (RMSD=9.8ppm) between the two datasets separately appear at SDZ and LFS stations, and the
 525 smallest values ($R'=0.68$, RMSD=4.4ppm, and MD=3.7ppm) are found at the WLG station.

526 The distribution of CO₂ mole fractions from the GOSAT L3 products over China during

527 September 2009–August 2011 shows significant seasonal difference (low in summer and high
528 in winter) and spatial gradient (low in the western part and high in the eastern part of China).
529 Through the comparison of the two-year averages, column CO₂ is found lower than ground-
530 based CO₂, but at WLG, both of them have the lowest CO₂ mole fraction. The lowest (~4 ppm)
531 and largest (~8 ppm) differences between the two datasets appear at WLG and LFS stations,
532 respectively. Compared with the winter situation, the CO₂ mole fraction and its difference
533 between full column and surface measurement are smaller in summer. The differences of full
534 column CO₂ between these stations are also much smaller than their surface observations. In
535 winter, the maximum of ground-based CO₂ mole fractions and the greatest difference between
536 the two datasets appear at the LFS station, perhaps due to the winter heating in Northeast China.
537 These varying results are probably induced by uptakes and emissions by vegetation and soils
538 and anthropogenic emissions.

539 In addition, footprints, which can reflect emission sensitivity, are distributed in different
540 regions for different seasons and sites due to the summer and winter monsoons. The linear
541 regression analysis of flask data and simulated results reveals that the CO₂ patterns at these
542 stations can be simulated well by the CT2015 model. The CO₂ background mole fractions at
543 the four stations have been extracted from qualified CO₂ simulation results by the screening
544 method of Robust Extraction of Background Signal and then smoothed by the curve-fitting
545 method.

546 While exploring the source–sink regional representativeness of the monthly CO₂ fitted
547 background mole fractions at the WMO/GAW stations, representative areas are found using
548 footprints and emissions. Smaller representative areas appear at the SDZ and LFS stations with
549 the larger of the best footprint threshold values, but the opposite case occurs at the WLG and
550 LAN stations. The representative areas are larger in summer than in winter at the WLG and
551 SDZ stations, but the situation is opposite at the LAN and LFS stations. The distributions of
552 best threshold area are significantly different whether in summer or winter or among different
553 stations. The representative areas for CO₂ background mole fractions at the WLG, SDZ, LAN,
554 and LFS stations are distributed mainly in the western part of China, the Beijing–Tianjin–Hebei
555 region, the eastern part of China, and northeast China, respectively.

556 The source and sink in the representative regions were also compared. The flux has obvious

557 seasonal cycles with similar trends but different seasonal variation ranges at the four stations.
558 There are also some differences in the time of strongest carbon sink for the different stations.
559 The intensities of CO₂ source and sink are the weakest at WLG; the strongest CO₂ source of
560 2.85 μ•mol/(m².s) with stronger CO₂ sink occurs at SDZ; the CO₂ source and sink at LAN are
561 strong and close to the intensities at SDZ; and the strongest CO₂ sink of -9.83 μ•mol/(m².s)
562 appears at LFS with weaker source. The uncertainties of the CO₂ fluxes are different at different
563 stations in different months and source-sink sectors. Overall, WLG is a carbon sink in the
564 representative area, but the other three stations present stronger carbon sources during the most
565 period of the year. The different atmospheric conditions, vegetation types, and economic zones
566 represented by the four stations contribute to the different sources and sinks in the
567 representative areas. Thus, the atmospheric CO₂ background mole fractions at the four
568 WMO/GAW stations in China can play a significant role in understanding regional CO₂ source-
569 sink characteristics and patterns over China, although it is necessary to reduce the uncertainty
570 of CO₂ source and sink in the best threshold region in future's studies.

571 **Acknowledgments**

572 This work was supported by the National Natural Science Foundation of China (Grant No.
573 41505123), the International S&T Cooperation Program of the MOST (Grant No. 2015DFG21960),
574 the National Key Research and Development Program of China (Grant No.2016YFA0601304), and
575 the CAMS Fundamental Research Funds (Grant No. 2015Y002).

576 We are grateful to all of the staff who work at the WMO/GAW stations in China for collecting
577 the flask air samples, and to the Greenhouse Gases Research Laboratory of the China
578 Meteorological Administration (CMA) for sample analysis. We appreciate Ed Dlugokencky, Andy
579 Crotwell, and Kirk Thoning of NOAA for their support of the research measurements. We also thank
580 the National Oceanic and Atmospheric Administration (NOAA) for providing the CT2015 data, the
581 Norwegian Institute for Air Research for providing the FLEXPART model, and the Japan Aerospace
582 Exploration Agency/National Institute for Environmental Studies/Ministry of the Environment
583 (JAXA/NIES/MOE) for the GOSAT products.

584 **References**

585 An, X., Yao, B., Li, Y., Li, N., Zhou, L., 2014. Tracking source area of Shangdianzi station using Lagrangian
586 particle dispersion model of FLEXPART. *Meteorological Applications* 21, 466-473.

587 An, X., Zhou, L., Yao, B., Xu, L., Ma, L., 2012. Analysis on source features of halogenated gases at
588 Shangdianzi regional atmospheric background station. *Atmospheric Environment* 57, 91-100.

589 Aumann, H.H., Chahine, M.T., Gautier, C., Goldberg, M., Kalnay, E., McMillin, L., Revercomb, H.,
590 Rosenkranz, P.W., Smith, W.L., Staelin, D., Strow, L., Susskind, J., 2003. AIRS/AMSU/HSB on the aqua
591 mission: design, science objectives, data products, and processing systems. *IEEE Transactions on*
592 *Geoscience and Remote Sensing* 41, 253-264.

593 Baker, D.F., Bösch, H., Doney, S.C., O'Brien, D., Schimel, D.S., 2010. Carbon source/sink information
594 provided by column CO₂ measurements from the Orbiting Carbon Observatory. *Atmospheric*
595 *Chemistry and Physics* 10, 4145-4165.

596 Ballantyne, A.P., Alden, C.B., Miller, J.B., Tans, P.P., White, J.W., 2012. Increase in observed net carbon
597 dioxide uptake by land and oceans during the past 50 years. *Nature* 488, 70-72.

598 Boesch, H., Baker, D., Connor, B., Crisp, D., Miller, C., 2011. Global Characterization of CO₂ Column
599 Retrievals from Shortwave-Infrared Satellite Observations of the Orbiting Carbon Observatory-2
600 Mission. *Remote Sensing* 3, 270-304.

601 Bovensmann, H., Burrows, J.P., Buchwitz, M., Frerick, J., Noël, S., Rozanov, V.V., Chance, K.V., Goede,
602 A.P.H., 1999. SCIAMACHY: Mission Objectives and Measurement Modes. *Journal of the*
603 *Atmospheric Sciences* 56, 127-150.

604 Bréon, F.M., Ciais, P., 2010. Spaceborne remote sensing of greenhouse gas concentrations. *Comptes*
605 *Rendus Geoscience* 342, 412-424.

606 Buchwitz, M., Noël, S., Bramstedt, K., Rozanov, V.V., Eisinger, M., Bovensmann, H., Tsvetkova, S., Burrows,
607 J.P., 2004. Retrieval of trace gas vertical columns from SCIAMACHY/ENVISAT near-infrared nadir
608 spectra: first preliminary results. *Advances in Space Research* 34, 809-814.

609 Chen, X., Wang, J., Liu, Y., Xu, X., Cai, Z., Yang, D., Yan, C.X., Feng, L., 2017. Angular dependence of aerosol
610 information content in CAPI/TanSat observation over land: Effect of polarization and synergy with
611 A-train satellites. *Remote Sensing of Environment* 196, 163-177.

612 Cheng, S., An, X., Zhou, L., Tans, P.P., Jacobson, A., 2017a. Atmospheric CO₂ at Waliguan station in China:
613 Transport climatology, temporal patterns and source-sink region representativeness. *Atmospheric*
614 *Environment* 159, 107-116.

615 Cheng, S., Wang, Y., An, X., 2017b. Temporal Variation and Source Identification of Black Carbon at Lin'an
616 and Longfengshan Regional Background Stations in China. *Journal of Meteorological Research* 31,
617 1070-1084.

618 Cheng, Y., An, X., Yun, F., Zhou, L., Liu, L., Fang, S., Xu, L., 2013. Simulation of CO₂ variations at Chinese
619 background atmospheric monitoring stations between 2000 and 2009: Applying a CarbonTracker
620 model. *Chinese Science Bulletin* 58, 3986-3993.

621 Chevallier, F., Deutscher, N.M., Conway, T.J., Ciais, P., Ciattaglia, L., Dohe, S., Fröhlich, M., Gomez-Pelaez,
622 A.J., Griffith, D., Hase, F., Haszpra, L., Krummel, P., Kyrö, E., Labuschagne, C., Langenfelds, R.,
623 Machida, T., Maignan, F., Matsueda, H., Morino, I., Notholt, J., Ramonet, M., Sawa, Y., Schmidt, M.,
624 Sherlock, V., Steele, P., Strong, K., Sussmann, R., Wennberg, P., Wofsy, S., Worthy, D., Wunch, D.,
625 Zimnoch, M., 2011. Global CO₂ fluxes inferred from surface air-sample measurements and from
626 TCCON retrievals of the CO₂ total column. *Geophysical Research Letters* 38, L24810.

627 Chevallier, F., Maksyutov, S., Bousquet, P., Bréon, F.M., Saito, R., Yoshida, Y., Yokota, T., 2009. On the
628 accuracy of the CO₂ surface fluxes to be estimated from the GOSAT observations. *Geophysical*
629 *Research Letters* 36, L19807.

630 Clerbaux, C., Boynard, A., Clarisse, L., George, M., Hadji-Lazaro, J., Herbin, H., Hurtmans, D., Pommier,

631 M., Razavi, A., Turquety, S., Wespes, C., Coheur, P.F., 2009. Monitoring of atmospheric composition
632 using the thermal infrared IASI/MetOp sounder. *Atmospheric Chemistry and Physics* 9, 6041-6054.

633 Cogan, A.J., Boesch, H., Parker, R.J., Feng, L., Palmer, P.I., Blavier, J.F.L., Deutscher, N.M., Macatangay, R.,
634 Notholt, J., Roehl, C., Warneke, T., Wunch, D., 2012. Atmospheric carbon dioxide retrieved from
635 the Greenhouse gases Observing SATellite (GOSAT): Comparison with ground-based TCCON
636 observations and GEOS-Chem model calculations. *Journal of Geophysical Research* 117, D21301.

637 Fang, S., Luan, T., Zhang, G., Wu, Y., Yu, D., 2015a. The determination of regional CO₂ mole fractions at
638 the Longfengshan WMO/GAW station: A comparison of four data filtering approaches.
639 *Atmospheric Environment* 116, 36-43.

640 Fang, S., Tans, P., Steinbacher, M., Zhou, L., Luan, T., 2015b. Comparison of the regional CO₂ mole fraction
641 filtering approaches at a WMO/GAW regional station in China. *Atmospheric Measurement*
642 *Techniques* 8, 5301-5313.

643 Fang, S., Tans, P.P., Steinbacher, M., Zhou, L., Luan, T., Li, Z., 2016. Observation of atmospheric CO₂ and
644 CO at Shangri-La station: results from the only regional station located at southwestern China.
645 *Tellus B: Chemical and Physical Meteorology* 68, 28506.

646 Fang, S., Zhou, L., Tans, P., Ciais, P., Steinbacher, M., Xu, L., Luan, T., 2014. In situ measurement of
647 atmospheric CO₂ at the four WMO/GAW stations in China. *Atmospheric Chemistry and Physics* 14,
648 2541-2554.

649 Frankenberg, C., Pollock, R., Lee, R.A.M., Rosenberg, R., Blavier, J.F., Crisp, D., O'Dell, C.W., Osterman,
650 G.B., Roehl, C., Wennberg, P.O., Wunch, D., 2015. The Orbiting Carbon Observatory (OCO-2):
651 spectrometer performance evaluation using pre-launch direct sun measurements. *Atmospheric*
652 *Measurement Techniques* 8, 301-313.

653 Houweling, S., Breon, F.M., Aben, I., Rödenbeck, C., Gloor, M., Heimann, M., Ciais, P., 2004. Inverse
654 modeling of CO₂ sources and sinks using satellite data: a synthetic inter-comparison of
655 measurement techniques and their performance as a function of space and time. *Atmospheric*
656 *Chemistry and Physics* 4, 523-538.

657 IPCC-AR5, 2013. *Climate Change 2013: the Physical Science Basis*. Working Group I Contribution to the
658 Fifth Assessment Report of the Intergovernmental Panel on Climate Change, Summary for
659 Policymakers.

660 Jiang, F., Wang, H., Chen, J., Zhou, L., Ju, W., Ding, A., Liu, L., Peters, W., 2013. Nested atmospheric
661 inversion for the terrestrial carbon sources and sinks in China. *Biogeosciences* 10, 5311-5324.

662 Jiang, X., Chahine, M.T., Olsen, E.T., Chen, L.L., Yung, Y.L., 2010. Interannual variability of mid-
663 tropospheric CO₂ from Atmospheric Infrared Sounder. *Geophysical Research Letters* 37, L13801.

664 Jiang, X., Crisp, D., Olsen, E., Kulawik, S., Miller, C., Pagano, T., Liang, M., Yung, Y., 2016. CO₂ annual and
665 semiannual cycles from multiple satellite retrievals and models. *Earth and Space Science* 3, 78-87.

666 Kulawik, S.S., Jones, D.B.A., Nassar, R., Irion, F.W., Worden, J.R., Bowman, K.W., Machida, T., Matsueda,
667 H., Sawa, Y., Biraud, S.C., Fischer, M.L., Jacobson, A.R., 2010. Characterization of Tropospheric
668 Emission Spectrometer (TES) CO₂ for carbon cycle science. *Atmospheric Chemistry and Physics* 10,
669 5601-5623.

670 Kuze, A., Suto, H., Nakajima, M., Hamazaki, T., 2009. Thermal and near infrared sensor for carbon
671 observation Fourier-transform spectrometer on the Greenhouse Gases Observing Satellite for
672 greenhouse gases monitoring. *Applied Optics* 48, 6716-6733.

673 Lauvaux, T., Pannekoek, O., Sarrat, C., Chevallier, F., Ciais, P., Noilhan, J., Rayner, P.J., 2009. Structure
674 of the transport uncertainty in mesoscale inversions of CO₂ sources and sinks using ensemble

675 model simulations. *Biogeosciences* 6, 1089-1102.

676 Lei, L., Guan, X., Zeng, Z., Zhang, B., Ru, F., Bu, R., 2014. A comparison of atmospheric CO₂ concentration
677 GOSAT-based observations and model simulations. *Science China Earth Sciences* 57, 1393-1402.

678 Li, C., Zhou, L., Qin, D., Liu, L., Qin, X., Wang, Z., Ren, J., 2014. Preliminary study of atmospheric carbon
679 dioxide in a glacial area of the Qilian Mountains, west China. *Atmospheric Environment* 99, 485-
680 490.

681 Li, R., Zhang, M., Chen, L., Kou, X., Skorokhod, A., 2017. CMAQ simulation of atmospheric CO₂
682 concentration in East Asia: Comparison with GOSAT observations and ground measurements.
683 *Atmospheric Environment* 160, 176-185.

684 Liu, D., Lei, L., Guo, L., Zeng, Z., 2015. A Cluster of CO₂ Change Characteristics with GOSAT Observations
685 for Viewing the Spatial Pattern of CO₂ Emission and Absorption. *Atmosphere* 6, 1695-1713.

686 Liu, L., Zhou, L., Vaughn, B., Miller, J., Brand, W., Rothe, M., Xia, L., 2014. Background variations of
687 atmospheric CO₂ and carbon-stable isotopes at Waliguan and Shangdianzi stations in China. *Journal*
688 *of Geophysical Research: Atmospheres* 119, 5602-5612.

689 Liu, L., Zhou, L., Zhang, X., Wen, M., Zhang, F., Yao, B., Fang, S., 2009. The characteristics of atmospheric
690 CO₂ concentration variation of four national background stations in China. *Science in China Series*
691 *D: Earth Sciences* 52, 1857-1863.

692 Liu, S., Zhou, T., Wei, L., Shu, Y., 2012. The spatial distribution of forest carbon sinks and sources in China.
693 *Chinese Science Bulletin* 57, 1699-1707.

694 Lu, Z., Streets, D., Zhang, Q., Wang, S., 2012. A novel back-trajectory analysis of the origin of black carbon
695 transported to the Himalayas and Tibetan Plateau during 1996-2010. *Geophysical Research Letters*
696 39, L01809.

697 Masarie, K., Langenfelds, R., Allison, C., Conway, T., Dlugokencky, E., Francey, R., Novelli, P., Steele, L.,
698 Tans, P., Vaughn, B., White, J., 2001. NOAA/CSIRO Flask Air Intercomparison Experiment: A strategy
699 for directly assessing consistency among atmospheric measurements made by independent
700 laboratories. *Journal of Geophysical Research: Atmospheres* 106, 20445-20464.

701 Miao, R., Lu, N., Yao, L., Zhu, Y., Wang, J., Sun, J., 2013. Multi-Year Comparison of Carbon Dioxide from
702 Satellite Data with Ground-Based FTS Measurements (2003–2011). *Remote Sensing* 5, 3431-3456.

703 Miller, C.E., Crisp, D., DeCola, P.L., Olsen, S.C., Randerson, J.T., Michalak, A.M., Alkhaled, A., Rayner, P.,
704 Jacob, D.J., Suntharalingam, P., Jones, D.B.A., Denning, A.S., Nicholls, M.E., Doney, S.C., Pawson, S.,
705 Boesch, H., Connor, B.J., Fung, I.Y., O'Brien, D., Salawitch, R.J., Sander, S.P., Sen, B., Tans, P., Toon,
706 G.C., Wennberg, P.O., Wofsy, S.C., Yung, Y.L., Law, R.M., 2007. Precision requirements for space-
707 based X_{co2} data. *Journal of Geophysical Research* 112, D10314.

708 Nassar, R., Jones, D.B.A., Kulawik, S.S., Worden, J.R., Bowman, K.W., Andres, R.J., Suntharalingam, P.,
709 Chen, J.M., Brenninkmeijer, C.A.M., Schuck, T.J., Conway, T.J., Worthy, D.E., 2011. Inverse modeling
710 of CO₂ sources and sinks using satellite observations of CO₂ from TES and surface flask
711 measurements. *Atmospheric Chemistry and Physics* 11, 6029-6047.

712 O'Dell, C., Connor, B., Bösch, H., O'Brien, D., Frankenberg, C., Castano, R., Christi, M., Eldering, D., Fisher,
713 B., Gunson, M., McDuffie, J., Miller, C., Natraj, V., Oyafuso, F., Polonsky, I., Smyth, M., Taylor, T.,
714 Toon, G., Wennberg, P., Wunch, D., 2012. The ACOS CO₂ retrieval algorithm – Part 1: Description
715 and validation against synthetic observations. *Atmospheric Measurement Techniques* 5, 99-121.

716 Peters, G., Marland, G., Le Quéré, C., Boden, T., Canadell, J., Raupach, M., 2011. Rapid growth in CO₂
717 emissions after the 2008–2009 global financial crisis. *Nature Climate Change* 2, 2-4.

718 Peters, W., Jacobson, A., Sweeney, C., Andrews, A., Conway, T., Masarie, K., Miller, J., Bruhwiler, L., Petron,

719 G., Hirsch, A., Worthy, D., van der Werf, G., Randerson, J., Wennberg, P., Krol, M., Tans, P., 2007. An
720 atmospheric perspective on North American carbon dioxide exchange: CarbonTracker. Proc. Natl.
721 Acad. Sci. U. S. A. 104, 18925-18930.

722 Piao, S., Fang, J., Ciais, P., Peylin, P., Huang, Y., Sitch, S., Wang, T., 2009. The carbon balance of terrestrial
723 ecosystems in China. Nature 458, 1009-1013.

724 Pillai, D., Gerbig, C., Marshall, J., Ahmadov, R., Kretschmer, R., Koch, T., Karstens, U., 2010. High
725 resolution modeling of CO₂ over Europe: implications for representation errors of satellite
726 retrievals. Atmospheric Chemistry and Physics 10, 83-94.

727 Pu, J., Xu, H., He, J., Fang, S., Zhou, L., 2014. Estimation of regional background concentration of CO₂ at
728 Lin'an Station in Yangtze River Delta, China. Atmospheric Environment 94, 402-408.

729 Reuter, M., Bovensmann, H., Buchwitz, M., Burrows, J.P., Connor, B.J., Deutscher, N.M., Griffith, D.W.T.,
730 Heymann, J., Keppel-Aleks, G., Messerschmidt, J., Notholt, J., Petri, C., Robinson, J., Schneising, O.,
731 Sherlock, V., Velasco, V., Warneke, T., Wennberg, P.O., Wunch, D., 2011. Retrieval of atmospheric
732 CO₂ with enhanced accuracy and precision from SCIAMACHY: Validation with FTS measurements
733 and comparison with model results. Journal of Geophysical Research 116, D04301.

734 Ruckstuhl, A., Henne, S., Reimann, S., Steinbacher, M., Vollmer, M., O'Doherty, S., Buchmann, B., Hueglin,
735 C., 2012. Robust extraction of baseline signal of atmospheric trace species using local regression.
736 Atmospheric Measurement Techniques 5, 2613-2624.

737 Stohl, A., Forster, C., Frank, A., Seibert, P., Wotawa, G., 2005. Technical note: The Lagrangian particle
738 dispersion model FLEXPART version 6.2. Atmos. Chem. Phys. 5, 2461-2474.

739 Streets, D., Canty, T., Carmichael, G., de Foy, B., Dickerson, R., Duncan, B., Edwards, D., Haynes, J., Henze,
740 D., Houyoux, M., Jacob, D., Krotkov, N., Lamsal, L., Liu, Y., Lu, Z., Martin, R., Pfister, G., Pinder, R.,
741 Salawitch, R., Wecht, K., 2013. Emissions estimation from satellite retrievals: A review of current
742 capability. Atmospheric Environment 77, 1011-1042.

743 Sun, Z., Wang, X., Yamamoto, H., Tani, H., Zhong, G., Yin, S., 2018. An attempt to introduce atmospheric
744 CO₂ concentration data to estimate the gross primary production by the terrestrial biosphere and
745 analyze its effects. Ecological Indicators 84, 218-234.

746 Tangborn, A., Strow, L.L., Imbiriba, B., Ott, L., Pawson, S., 2013. Evaluation of a new middle-lower
747 tropospheric CO₂ product using data assimilation. Atmospheric Chemistry and Physics 13, 4487-
748 4500.

749 Tans, P., Thoning, K., Elliott, W., Conway, T., 1989. Background atmospheric CO₂ patterns from weekly
750 flask samples at Barrow, Alaska: optimal signal recovery and error estimates, NOAA Technical
751 Memorandum ERL ARL-173. Environmental Research Laboratories, Boulder, pp. 112-131.

752 Thoning, K., Tans, P., Komhyr, W., 1989. Atmospheric carbon dioxide at Mauna Loa observatory 2.
753 Analysis of the NOAA GMCC data, 1974-1985. Journal of Geophysical Research Atmospheres 94,
754 8549-8565.

755 Wang, X., Zhang, X., Zhang, L., Gao, L., Tian, L., 2015. Interpreting seasonal changes of low-tropospheric
756 CO₂ over China based on SCIAMACHY observations during 2003–2011. Atmospheric Environment
757 103, 180-187.

758 Xia, L., Zhou, L., Tans, P., Liu, L., Zhang, G., Wang, H., Luan, T., 2015. Atmospheric CO₂ and its δ¹³C
759 measurements from flask sampling at Lin'an regional background station in China. Atmospheric
760 Environment 117, 220-226.

761 Xu, B., Li, J., Liu, Q., Xin, X., Zeng, Y., Yin, G., 2015. Review of methods for evaluating representativeness
762 of ground station observations. Journal of Remote Sensing 19, 703-718 (In Chinese with English

763 Abstract).

764 Xu, J., Wang, Z., Yu, G., Sun, W., Qin, X., Ren, J., Qin, D., 2013. Seasonal and diurnal variations in aerosol
765 concentrations at a high-altitude site on the northern boundary of Qinghai-Xizang Plateau.
766 *Atmospheric Research* 120-121, 240-248.

767 Xu, Y., Ke, C., Zhan, W., Li, H., Yao, L., 2017. Variations in satellite-derived carbon dioxide over different
768 regions of China from 2003 to 2011. *Atmospheric Environment* 150, 379-388.

769 Yokota, T., Yoshida, Y., Eguchi, N., Ota, Y., Tanaka, T., Watanabe, H., Maksyutov, S., 2009. Global
770 Concentrations of CO₂ and CH₄ Retrieved from GOSAT: First Preliminary Results. *SOLA* 5, 160-163.

771 Yoshida, Y., Ota, Y., Eguchi, N., Kikuchi, N., Nobuta, K., Tran, H., Morino, I., Yokota, T., 2011. Retrieval
772 algorithm for CO₂ and CH₄ column abundances from short-wavelength infrared spectral
773 observations by the Greenhouse gases observing satellite. *Atmospheric Measurement Techniques*
774 4, 717-734.

775 Zhang, F., Zhou, L., Conway, T., Tans, P., Wang, Y., 2013a. Short-term variations of atmospheric CO₂ and
776 dominant causes in summer and winter: Analysis of 14-year continuous observational data at
777 Waliguan, China. *Atmospheric Environment* 77, 140-148.

778 Zhang, F., Zhou, L., 2013. Implications for CO₂ emissions and sinks changes in western China during
779 1995–2008 from atmospheric CO₂ at Waliguan. *Tellus B* 65, 19576.

780 Zhang, H., Chen, B., Machida, T., Matsueda, H., Sawa, Y., Fukuyama, Y., Langenfelds, R., van der Schoot,
781 M., Xu, G., Yan, J., Cheng, M., Zhou, L., Tans, P., Peters, W., 2014a. Estimating Asian terrestrial
782 carbon fluxes from CONTRAIL aircraft and surface CO₂ observations for the period 2006-2010.
783 *Atmospheric Chemistry and Physics* 14, 5807-5824.

784 Zhang, H., Chen, B., van der Laan-Luijkx, I., Chen, J., Xu, G., Yan, J., Zhou, L., Fukuyama, Y., Tans, P., Peters,
785 W., 2014b. Net terrestrial CO₂ exchange over China during 2001-2010 estimated with an ensemble
786 data assimilation system for atmospheric CO₂. *Journal of Geophysical Research: Atmospheres* 119,
787 3500-3515.

788 Zhang, J., Wang, C., Liu, L., Guo, H., Liu, G., Li, Y., Deng, S., 2014c. Investigation of carbon dioxide emission
789 in China by primary component analysis. *Sci. Total Environ.* 472, 239-247.

790 Zhang, L., Jiang, H., Zhang, X., 2015. Comparison analysis of the global carbon dioxide concentration
791 column derived from SCIAMACHY, AIRS, and GOSAT with surface station measurements.
792 *International Journal of Remote Sensing* 36, 1406-1423.

793 Zhang, Z., Jiang, H., Liu, J., Ju, W., Zhang, X., 2013b. Effect of heterogeneous atmospheric CO₂ on
794 simulated global carbon budget. *Global and Planetary Change* 101, 33-51.

795 Zhou, C., Shi, R., Liu, C., Gao, W., 2013. A correlation analysis of monthly mean CO₂ retrieved from the
796 Atmospheric Infrared Sounder with surface station measurements. *International Journal of*
797 *Remote Sensing* 34, 8710-8723.

798 Zhou, L., Conway, T., White, J., Mukai, H., Zhang, X., Wen, Y., Li, J., MacClune, K., 2005. Long-term record
799 of atmospheric CO₂ and stable isotopic ratios at Waliguan Observatory: Background features and
800 possible drivers, 1991-2002. *Global Biogeochemical Cycles* 19, GB3021.

801 Zhou, L., Tang, J., Wen, Y., Yan, P., Li, J., Zhang, X., 2003. The impact of local winds and long-range
802 transport on the continuous carbon dioxide record at Mount Waliguan, China. *Tellus B* 55, 145-158.

803 Zhou, L., White, J., Conway, T., Mukai, H., MacClune, K., Zhang, X., Wen, Y., Li, J., 2006. Long-term record
804 of atmospheric CO₂ and stable isotopic ratios at Waliguan Observatory: Seasonally averaged 1991-
805 2002 source/sink signals, and a comparison of 1998-2002 record to the 11 selected sites in the
806 Northern Hemisphere. *Global Biogeochemical Cycles* 20, GB2001.